Organic Electronics 67 (2019) 1–9

Contents lists available at ScienceDirect

Organic Electronics

journal homepage: www.elsevier.com/locate/orgel

Doping induced performance enhancement in inverted small molecule organic photodiodes operating below 1V reverse bias - Towards compatibility with CMOS for imaging applications

Himanshu Shekhar[a], Vincent Lami[c], Olga Solomeshch[a], Amos Fenigstein[b], Leitner Tomer[b], Lavi Becky[b], Yana Vaynzof[c], Nir Tessler[a,*]

[a] Microelectronics and Nanoelectronics Centers, Electrical Engineering Department, Technion Israel Institute of Technology, Haifa, 32000, Israel
[b] TowerJazz, Tower Semiconductor Ltd., Migdal Haemek, 2310502, Israel
[c] Kirchhoff Institute for Physics and Centre for Advanced Materials, Im Neuenheimer Feld 227, Heidelberg, 69120, Germany

ARTICLE INFO

Keywords:
Organic photodiode
Titanium nitride
Interface engineering
Cathode buffer layer
Doping
CMOS

ABSTRACT

Organic photodiodes (OPDs) offer a myriad of advantages over conventional inorganic photodetectors, making them particularly attractive for imaging application. One of the key challenges preventing their utilization is the need for their integration into the standard CMOS processing. Herein, we report a CMOS-compatible top-illuminated inverted small molecule bi-layer OPD with extremely low dark leakage current. The device utilizes a titanium nitride (TiN) bottom electrode modified by a [6,6]-phenyl C_{61} butyric acid methyl ester (PCBM) cathode buffer layer (CBL). We systemetically show that doping the CBL enhances device's low voltage (below 1 V reverse bias) photoresponse by increasing the linear dynamic range (LDR) and making the bandwidth of the photodidoe broader without compromising the leakage current. The optimized device exhibits a dark leakage current of only $\sim 6 \times 10^{-10}$ A/cm^2 at -0.5 V. The external quantum efficiency (EQE) at 500 nm reaches 23% with a calculated specific detectivity as high as 7.15×10^{12} cm Hz$^{1/2}$/W (Jones). Also the LDR approaches 140 dB and the bandwidth is about 400 kHz, at -0.5 V bias. The proposed device structure is fully compatible with CMOS processing and can be integrated onto a CMOS readout circuit offering the potential to be applied in high-performance large-scale imaging arrays.

1. Introduction

Organic photodiodes (OPDs) are a promising alternative to traditional inorganic photodetectors for application in detection and imaging due to their advantageous properties [1–5]. These properties include, among others, tunable optical response, high absorption coefficients and the possibility to be fabricated on a variety of different substrates. A range of such OPDs based, for example, on small molecules, polymers as well as organic-inorganic active layers have already been investigated for imaging technologies resulting in promising device performance and characteristics [6–10].

The beneficial properties mentioned above offer the opportunity to envisage imagers that combine the advantages of organic materials with established silicon technologies. Several examples exist, in which OPDs were successfully integrated on the backplane of organic [11], metal-oxide [12], and a-Si:H [13] thin-film transistor (TFT) readout circuits, mostly employed in large-area applications such as x-ray imagers. Recently, a proof-of-concept OPD integrated on the backplane of a CMOS readout integrated circuit (ROIC) has been demonstrated by Mori et al., [14]. With such hybrid imagers based on a CMOS backplane it is expected to have high switching speed and reduced pixel and readout noise as compared to a-Si:H based imaging devices [15]. However, such OPD devices would need to be CMOS-compatible, introducing significant challenges due to the fact that the device bottom electrode must be opaque and is strictly restricted by the CMOS process flow. For example, while aluminium (Al) is a common material in the CMOS flow and could serve as a cathode in an OPD, it is highly reactive and quickly forms a thin native oxide layer upon exposure to ambient atmosphere [16,17] making it difficult for use as a bottom electrode. To counter this issue, Baierl et al. proposed etching the Al contact pads just prior to the organic layer deposition [18], while Yen et al. coated the Al electrodes with a thin conductive metal-oxide [19]. While these approaches allowed the fabrication of OPDs over Al pads, they complicate the overall device fabrication by the necessity of addition of processing

* Corresponding author.
E-mail address: nir@ef.technion.ac.il (N. Tessler).

https://doi.org/10.1016/j.orgel.2019.01.002
Received 11 November 2018; Received in revised form 31 December 2018; Accepted 2 January 2019
Available online 03 January 2019

and patterning steps.

Another material which is part of a CMOS process-flow, but is rarely explored as an electrode, is titanium nitride (TiN). TiN offers chemical inertness and excellent electrical properties [20], making it very promising for utilization as an electrode. However, a key drawback of physical vapour deposited (PVD) TiN films is their large surface roughness with peak height reaching several tens of nanometres [21]. These topological features on the surface of TiN might be detrimental to thin organic photoactive layers. Moreover, they are likely to serve as a potential source of leakage current by forming shunt paths between the top and bottom electrodes. One approach, demonstrated by Mori et al., is based on a chemical mechanical polishing (CMP) technique to create a completely flat Ti-based bottom electrode [14], however, this method requires additional processing and, therefore, increases complexity and cost. Another key requirement from the TiN electrode is related to the quality of the interface that it forms with the organic layers. An interfacial layer that forms a good electrical contact with the underneath TiN electrode is important for the efficient collection of the photogenerated electrons. Malinowski et al. showed that this can be taken care of by inserting a n-type metal-oxide semiconducting (TiO_X or ZnO) interlayer between the TiN and the active layer [22], however this approach is complicated by the high processing temperature (> 400 °C) of these metal oxides [23,24] and the need for further process optimization prior to their integration into imaging systems.

An alternative approach that would mitigate above mentioned issues of TiN is the insertion of a doped interlayer between the bottom electrode and the photoactive layer. Such a layer can smoothen the rough surface of TiN and isolate the photoactive layer from the rough surface of TiN. Additionally, it also improves electron transport and injection by providing an advantageous energetic alignment between the active layer and the bottom electrode. However, to be suitable for image-sensing applications, the interlayer must also guarantee that the diode leakage current and electrical cross-talk between in-plane pixels are not compromised, while improving electrical contact between the bottom electrode and the photoactive layer [25].

In this work, we demonstrate that TiN can be successfully utilized as a bottom cathode contact to realize a CMOS compatible high performance OPD based on a bi-layer C_{70}/TAPC active layer. Due to the low operation voltage of CMOS circuits (2–3 V) the bias available to the photodiode may be below 2 V. As the signal readout is based on charge integration mediated reduction of the bias across the photodiode, the range -1 V to 0 V becomes a significant part of the photodiodes dynamic range. Hence, in this paper we also place an emphasis on the performance at below 1 V reverse bias (i.e. -1 V–0 V). We show that a (4-(1,3-dimethyl-2,3-dihydro-1H-benzoimidazol-2-yl)phenyl)dimethylamine (N-DMBI) doped [6,6]-phenyl C61 butyric acid methyl ester (PCBM) cathode modifier allows both improved electron transport and loss reduction, as well as suppressing reverse bias leakage current. We optimize the interlayer thickness and doping level and demonstrate that it can be patterned based on the requirements of a CMOS process. Considering the total thickness of the active layer, the optimized OPD exhibits an impressive dark leakage current of only $\sim 6 \times 10^{-10}$ A/cm^2 at -0.5 V and $\sim 1 \times 10^{-9}$ A/cm^2 at -1 V. The device shows a specific detectivity as high as 7.15×10^{12} cm Hz$^{1/2}$/W and a linear dynamic range (LDR) of 140 dB at -0.5 V bias. At this low bias, the bandwidth is 388 kHz. Our work significantly advances the engineering of OPD devices, making them fully compatible with CMOS processing which will allow their future integration into industrial imaging applications.

2. Experimental

Organic Photodiode Fabrication: OPDs were fabricated on Si/SiO_2/TiN substrates where TiN is acting as bottom contact cathode. To avoid any perimeter leakage, the edges of the patterned TiN were covered with 700 nm thick polyimide layer leaving a diode active area of 18.4 mm^2. Next, a 80 nm thick layer of N-DMBI (Sigma 99.9%) doped PCBM (NANO-C 99.5%) was deposited by spin-coating. For this purpose, a 28 mg/ml solution of PCBM dissolved in CB was stirred and heated (at 70 °C) for 24 h; after that the solution was filtered (0.2 μm PTFE) and mixed with N-DMBI solution (in CB) at different molar %, and left overnight to mix well before spin coating. The films were spin-coated inside a nitrogen-filled glovebox and annealed at 75 °C for 30 min to ensure activation of the N-DMBI dopant. Directly afterwards, a 50 nm thick film of C_{70} (Lumtec) and a 50 nm thick film of TAPC (Lumtec) were thermally evaporated to serve as acceptor/donor bi-layer. Finally, a tri-layer anode consisting of 10 nm thick film of Molybdenum trioxide (MoO_3, Sigma 99.99%), 12 nm thick silver (Ag) and a 32 nm thick MoO_3 was evaporated. *Organic Photodiode Characterization:* Dark current-voltage of OPDs were characterized with a semiconductor parameter analyzer (B1500 A, Agilent Technologies) inside a nitrogen-filled glovebox. Intensity-dependent photocurrent was measured using a white light emitting diode matrices, whose intensity was controlled by the bias current. Appropriate optical density (OD) filters were used to extend the intensity range (~5 orders of magnitude) from $\sim 3 \times 10^{-5}$ Sun to ~3 Sun intensity. Spectrally resolved EQE was performed outside the glove box with measured samples kept in nitrogen atmosphere inside a holder. Light from the monochromator (Cornerstone™ 130) was chopped at 80 Hz, and the signal was read using a lock-in amplifier (EG & G 7265). Frequency measurements were conducted using a green light emitting diode (LED) modulated by a square pulse using AFG3252 Tektronix, waveform generator. The dynamic photocurrent response of the OPDs were recorded using a digital oscilloscope (DPO3034 Tektronix). *Field-Effect Transistor Fabrication and Characterization:* Organic field-effect transistors (OFETs) were fabricated on highly doped silicon Si^{++} substrates serving as gate, with a 100 nm thick SiO_2 insulating layer as dielectric. Spin-coated films (~30 nm) of undoped and N-DMBI doped PCBM were annealed in a nitrogen-filled oven for 15 h at 75 °C as reported in literature [26,27] (at a later stage we found that 30min would be sufficient and hence 30min was used for the photodiode fabrication). Finally, the devices were completed by a 30 nm calcium (Ca)/100 nm aluminium (Al) source-drain contacts which were thermally evaporated through a shadow mask. The electrical characterization of as-fabricated OFETs were done using a semiconductor parameter analyzer (B1500 A, Agilent Technologies) inside a nitrogen-filled glovebox. *Atomic Force and Kelvin Probe Microscopy:* Surface morphology images were acquired using a MFP-3D Infinity atomic force microscope (AFM) operated in tapping mode. For the surface potential energy images of TiN surface the AFM was operated in kelvin probe force microscopy (KPFM) imaging mode. *Optical Characterization*: Transmittance of glass/MoO_3 (10 nm)/Ag (12 nm)/MoO_3 (32 nm) tri-layer electrode stack was measured using a UV–Vis–NIR spectrophotometer (Cary 5000, Agilent) in air. *Ellipsometry*: The ellipsometry measurements of single films of MoO_3 and Ag films on glass were conducted by variable angle spectroscopic ellipsometry (VASE Ellipsometer J. A. Woollam Co.) model. *Ultraviolet Photoemission Spectroscopy (UPS)*: UPS measurement were performed using a double-differentially pumped He (Helium) discharge lamp ($h\upsilon$ = 21.22 eV) with a pass energy of 2 eV and a negative bias of -5 V in an ultrahigh vacuum system (ESCALAB 250 Xi). *Interlayer Patterning Experiments*: PCBM interlayer patterning was performed using i-line photolithography with a negative orthogonal photoresist (OSCoR 5001). After lithography, the PCBM surrounding the pixel area was removed by oxygen plasma reactive ion etching. Finally, the photoresist covering the pixel area was stripped in a stripper to leave PCBM on the active area only.

3. Results and discussion

3.1. TiN characterization and application as an electrode

To test the CMOS compatibility of the OPD, the complete device stack was fabricated on a test blanket wafer substrate of Si/SiO_2/TiN.

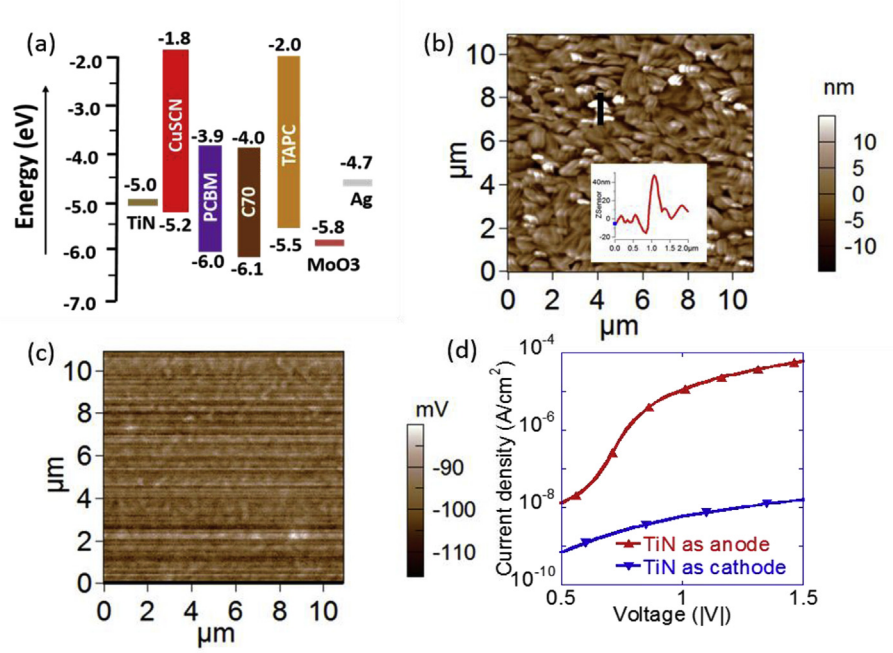

Fig. 1. (a) Energy levels of all the materials used in this work. (b) AFM image of the TiN surface showing the surface roughness. Presence of random spikes (white dots) protruding from the surface can be seen. (c) Potential difference distribution of TiN surface relative to the AFM tip material (tip coating material Ti/Ir). (d) Forward current-voltage characteristics for devices where TiN contact is used as anode (TiN/CuSCN/TAPC/C_{70}/BCP/Mg/Ag) and as cathode (TiN/PCBM/C_{70}/TAPC/MoO_3/Ag), respectively. The shown voltage range (here above 0.5 V) is chosen to highlight the diode's forward current only.

The compatibility of TiN as an OPD electrode was studied by fabricating an opaque device with the structure TiN/C_{70} (50 nm)/TAPC (50 nm)/MoO_3 (10 nm)/Ag (100 nm). The energetics of the different material layers are shown in Fig. 1a. All the devices with this structure suffered from either shorts or very high leakage current (see Supp. Info Fig. S1). This was to be expected based on the large surface roughness of TiN films. Indeed, Atomic Force Microscopy (AFM) images of TiN films (Fig. 1b) show a rough surface structure with a root mean square roughness of ~5.8 nm and random spikes larger than 50 nm. These spikes, in turn, are most likely to be the reason for the high leakage currents and shorts in the reference opaque devices. Kelvin probe force microscopy (KPFM) is an efficient method for surface potential calculation including polymeric surfaces. The measured contact potential difference (CPD) between the AFM tip and TiN surface (Fig. 1c) was used to extract the TiN work function using the following formula

$$\phi_{TiN} = \phi_{Tip} - qV_{CPD} \quad (1)$$

where ϕ_{TiN} is the potential of TiN, ϕ_{Tip} is the potential of the AFM tip (4.9 eV) and V_{CPD} is the potential difference between the two. The V_{CPD} was measured to be approximately −100 mV, resulting in an estimated TiN work function of (5.0 ± 0.1) eV, in agreement with previous reports [28]. It is often expected that these energetics of the TiN electrode should not have much influence over the photogenerated electron extraction especially in the context of OPDs where the devices operate under reverse bias. However, as we show below, this is not the case for low bias levels required by advanced circuits such as CMOS that typically operate in the range 2–3 V.

Coating the TiN electrode with an appropriate interlayer has the potential of transforming it into a cathode with improved surface structure and electronic properties [22]. In this work [6,6],-phenyl C61 butyric acid methyl ester (PCBM) was selected to act as a cathode interlayer due to several advantageous properties. Firstly, it can be easily deposited by solution processing and does not require high temperature processing. Secondly, PCBM is a commonly used electron transport layer, which would infiltrate the rough surface of TiN and act as a surface planarizer. Finally, it offers an ideal energetic alignment with the C_{70} layer within the active layer which should lower any losses at this interface [26]. While PCBM coating of TiN indeed resulted in smooth surface with root mean square roughness of ~1.35 nm (see Supp. Info. Fig. S2), devices with the structure TiN/PCBM (80 nm)/C_{70} (50 nm)/TAPC (50 nm)/MoO_3 (10 nm)/Ag (100 nm) resulted in a current-voltage characteristic with very low current in the forward bias direction (Fig. 1d). To eliminate the possibility that this is related to a formation of an insulating surface layer on top of TiN, we fabricated devices where TiN serves as anode with the structure TiN/CuSCN (80 nm)/TAPC (50 nm)/C_{70} (50 nm)/BCP (8 nm)/Mg (30 nm)/Ag (70 nm) where CuSCN is a hole transport layer [29]. Note that due to the TAPC/C70 heterojunction, the current crosses the junction through electron-hole recombination and thus a significant current will flow only if both electrons and holes will be injected. These devices showed efficient hole injection from TiN into CuSCN, suggesting that the poor electron injection efficiency from TiN into PCBM is not caused by the presence of an insulating surface layer, but rather by unfavourable energetic alignment. As shown above, the relatively high work function of TiN (5.0 ± 0.1 eV), allows for efficient hole injection into CuSCN (HOMO level ~5.2 eV), while in the case of PCBM (LUMO level ~3.9 eV), a large energetic barrier of ~1 eV is formed, significantly lowering the efficiency of electron injection.

Fig. 2 shows the photoresponse of top illuminated device structure TiN/PCBM (80 nm)/C_{70} (50 nm)/TAPC (50 nm)/MoO_3 (10 nm)/Ag (12 nm)/MoO_3 (32 nm) at two different biases. Details of the top transparent electrode MoO_3/Ag/MoO_3 is explained in the next section. Fig. 2a shows the spectrally resolved external quantum efficiency (EQE) of the above device at 0 and -1 V. Because of separate photocurrent channels for electrons and holes, bi-layer devices in general show very little reverse bias effect on the EQE. However, in this case the EQE increased by more than 30% (at 500 nm) to its short circuit value when a reverse bias of −1 V is applied. This rather significant increase in the EQE under reverse bias suggests inefficient charge extraction at low voltages. A similar behaviour was found in the photoresponse linearity measurement (Fig. 2b) of the same device. The light intensity response of the device at zero bias is sublinear, whereas applying an external bias improves the response which become almost linear at −1 V. Namely, while the use of PCBM as a planarizing layer did reduce the leakage current, the photo-response of the device was relatively poor in the -1 V to 0 V range.

3.2. Optimization of PCBM cathode modifier by doping

We note that in the current context, TiN cannot be used as anode

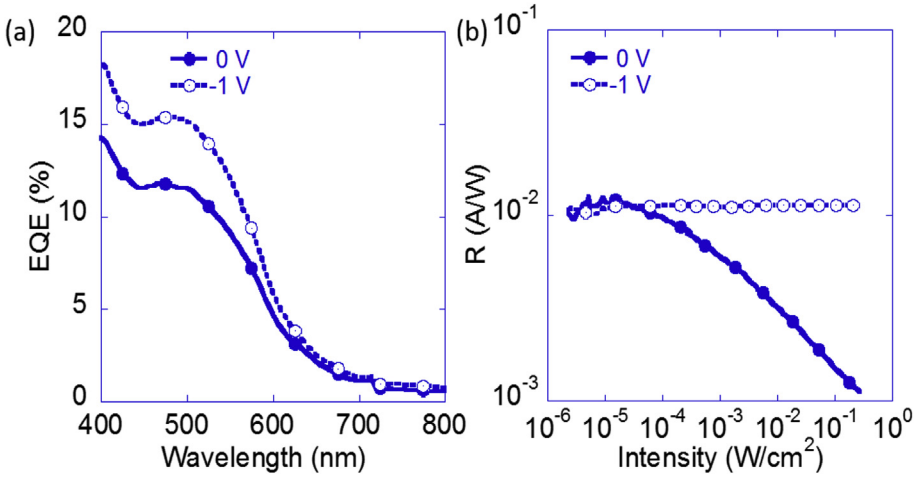

Fig. 2. Photoresponse of device structure TiN/PCBM (80 nm)/C_{70} (50 nm)/TAPC (50 nm)/MoO_3 (10 nm)/Ag (12 nm)/MoO3 (32 nm) showing (a) Spectral EQE response at short circuit and −1 V. (b) Responsivity of the same device at 0 and -1 V measured under white light illumination at different intensities.

due to the polarity of the bias imposed by the underneath CMOS readout circuit. As shown above, a large electron injection barrier is formed at the interface between TiN and PCBM, resulting in low efficiency of charge injection. Another limitation introduced by the PCBM interlayer is related to its relatively low conductivity. In order to planarize the rough TiN surface a relatively thick PCBM film (80 nm) has to be deposited, which hinders charge transport through this layer. This latter issue is particularly limiting for OPD devices that operate at low voltages.

Doping has been demonstrated to be an effective method to increase the conductivity of organic layers and to improve electrical contact between metal electrodes and organic layers [30,31]. We chose N-DMBI as an N-dopant as it can be easily introduced into the PCBM solution and has already been shown to be an efficient dopant of PCBM [27]. To confirm the efficacy of n-doping, we fabricated PCBM field-effect transistors with varying level of N-DMBI doping. Supp. Info. Fig. S3a shows characteristic transistor transfer curves for different molar concentrations of N-DMBI doped PCBM films. The curves exhibit a significant shift of the threshold voltage (V_t) to negative gate voltages with increasing doping level. This shift in V_t is attributed to the increased concentration of electrons across the semiconducting layer due to n-doping. To quantify the increase in electron conductivity of the doped films, two probe conductivity measurements were performed on both doped and undoped films (using Ca/Al as electrode). Supp. Info. Fig. S3b shows the extracted conductivity values for an 80 nm thick PCBM film as a function of N-DMBI % molar concentration. The conductivities of N-DMBI doped PCBM films increased significantly approaching 5×10^{-3} S/cm for 5% dopant concentration an increase of over 6 orders of magnitude higher when compared to undoped PCBM films ($\sim 10^{-9}$ S/cm).

To investigate the effect of doping on the energy level alignment at TiN/PCBM and PCBM/C_{70} interfaces, we performed ultraviolet photoelectron spectroscopy (UPS) measurements on both doped and undoped 20 nm thick PCBM films deposited on TiN. Upon coating with undoped PCBM, the TiN work function is reduced to 4.65 eV, which we interpret to arise from an interfacial dipole pointing into the TiN substrate. We attribute this to a corresponding ground state electron transfer from PCBM to TiN. The hole injection barrier for undoped PCBM is measured to be 1.4 eV (Fig. 3a), resulting in an ionization potential value of 6.05 eV, in excellent agreement with previous measurements [32]. Subtracting the 2.1 eV electronic bandgap of PCBM [33] allows us to estimate the position of the LUMO and the corresponding electron injection barrier. For the undoped case, this barrier is fairly large at 0.7 eV, in agreement with the low injection efficiency into PCBM described above. In the doped case (5% molar doping), a larger dipole of 0.9 eV is formed at the interface, resulting in a work function of 4.1 eV. It is possible that part of the level shift is also due to space charge effects [31]. We performed thickness dependence measurements that indicate that the potential contribution from space charge is ~0.1–0.15 eV. Since this value is very close to the experimental error of UPS (0.1 eV), we do not associate it with any significant space charge effects. The measured hole injection barrier is 1.85 eV, placing the Fermi level close to the LUMO level as expected upon n-doping. The corresponding electron injection barrier is only 0.25 eV, which should result in efficient charge injection into the doped layers. The advantageous interfacial alignment with C_{70} was confirmed by UPS measurements on TiN/PCBM/C_{70} films. The HOMO level of C_{70} shows a similar shift when deposited on doped PCBM layer (Fig. 3b), suggesting that the LUMOs of the PCBM and C_{70} layers remain aligned upon doping. The energetic alignment at the TiN/PCBM interface is summarized in Fig. 3c.

3.3. Anode design and characterization

The combination of the improved conductivity and improved energetic alignment makes doped PCBM layers an excellent candidate for application as cathode interlayers in inverted OPD. However it is important to keep in mind that the opaque nature of the bottom TiN electrode makes it necessary to develop a transparent top electrode that will allow the incoming photons to reach to the active part in the device.

Motivated by the recent progress on tri-layer dielectric-metal-dielectric (DMD) electrode structures [34–36], we fabricated a MoO_3/Ag/MoO_3 stacked electrode and adjusted the layer thicknesses to optimize the anode's optical and electrical properties. To model the electromagnetic field intensity distribution and consequently the light intensity transmitted through the DMD stack, ellipsometry measurements were performed to extract the complex refractive index parameters of the materials (Fig. 4a). We utilized an optical model based on transfer matrix formalism, which is suitable for multilayer systems [37]. Fig. 4b shows measured and simulated spectral transmission of an optimized stack of glass/MoO_3 (10 nm)/Ag (12 nm)/MoO_3 (32 nm). The measured and simulated transmission is relative to air and thus also includes reflection from the glass interface. Excluding the latter effect, the optimized tri-layer electrode stack has a peak transmission of ~88% at 500 nm. Fig. 4b also shows the measured absorption spectrum of thermally deposited C_{70} film on glass, demonstrating that the absorption peak at 500 nm coincides with the highest transmission region of the electrode stack.

In addition to the optimized optical properties, the DMD stack must have low enough sheet resistance to serve as an anode. It is also

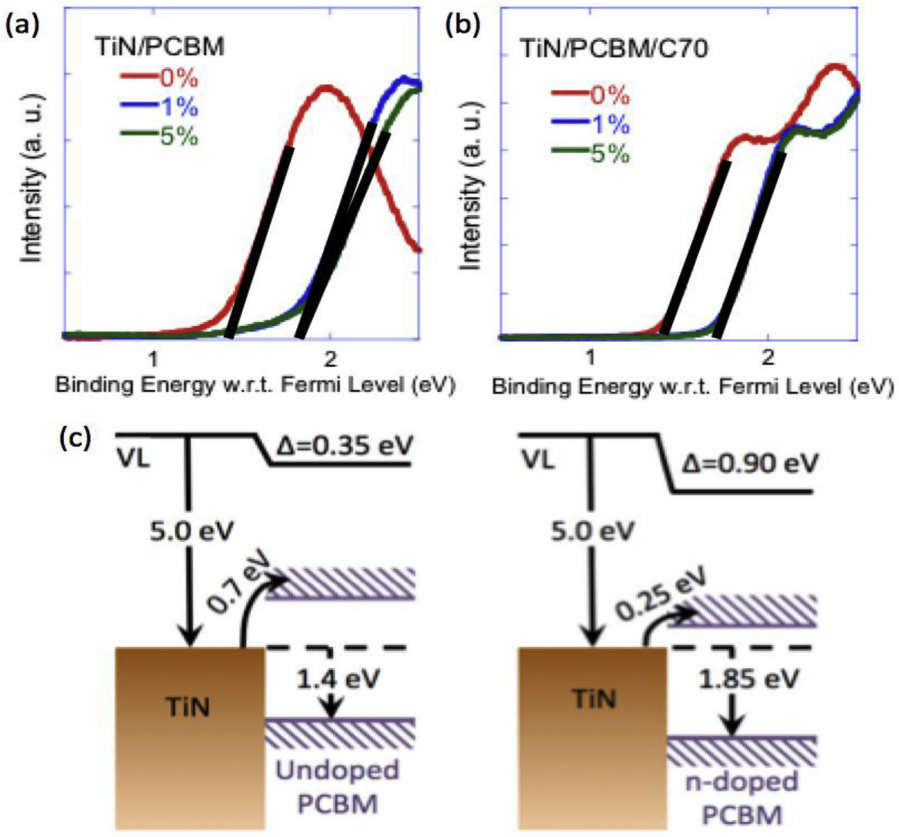

Fig. 3. UPS measurements showing the valence band spectra of (a) undoped and doped PCBM layers on TiN and of (b) thermally deposited C_{70} on top of doped and undoped PCBM layers. The black lines indicate HOMO level fits. (c) Schematic band energy diagram showing electron injection barrier at the TiN/PCBM interface for the undoped and for n-doped (5% molar doping) PCBM on the left and right, respectively.

desirable that the stack would be stable upon exposure to air and maintain its electrical properties. Fig. 4c shows the current voltage curve of the stack in the lateral direction measured immediately following fabrication and after 2 weeks of exposure to ambient atmosphere. The derived sheet resistance was found to be as low as ~9 Ω/sq making it suitable to serve as the anode of the OPD device.

3.4. Optimized photodiode structure and performance

Combining the optimized PCBM cathode modifier and the anode DMD structure, we fabricated OPD devices with the structure TiN/PCBM (80 nm)/C_{70} (50 nm)/TAPC (50 nm)/MoO_3 (10 nm)/Ag (12 nm)/MoO_3 (32 nm) with various doping levels of the PCBM layer (Fig. 5a). Fig. 5b shows the dark current-voltage characteristics of undoped, 0.25%, 1%, and 5% doped devices. We note that the doping % always refers to a molar % of doping and % doped device refers to the level of n-doped PCBM in the device. Devices with 5% doping level resulted in high reverse leakage currents and were therefore excluded from further characterization. The high leakage current in 5% doped devices is most likely to be associated with aggregation of N-DMBI stimulated complex formation at the surface of the doped PCBM films [27,38], as confirmed by the AFM and optical-microscope analysis (see Supp. Info. Fig. S4). For the 1% doped device the reverse bias leakage current at −1 V was in the range of 1–3 nA/cm^2. Measurements were conducted on devices fabricated in different batches to ensure that the results are reproducible. Supp. Info. Fig. S5 shows the dark current-voltage characteristics of 1% doped device from 4 different batch. To the best of our knowledge, these are one of the lowest leakage current values reported for inverted OPDs based on TiN electrodes. Fig. 5c shows the spectrally resolved external quantum efficiency (EQE) of undoped, 0.25% and 1% doped devices at zero bias. The 1% doped device yields an EQE of approximately 23% at 500 nm - nearly double to that of the undoped

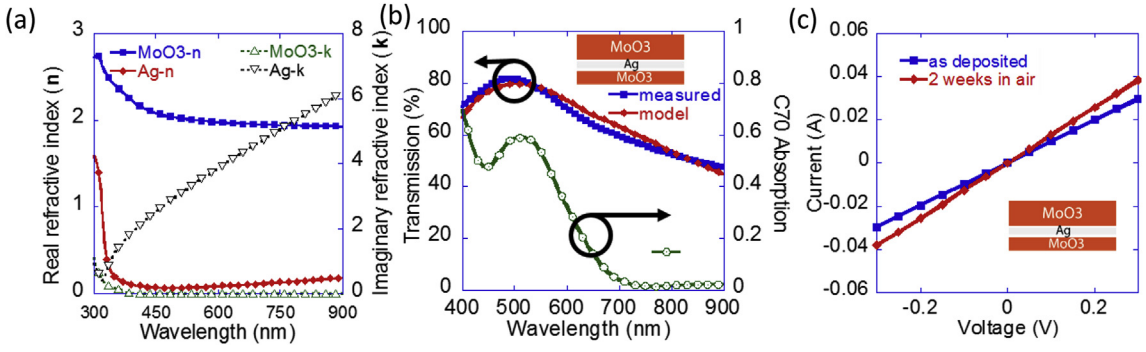

Fig. 4. (a) Real refractive index (n) and extinction coefficient (k) spectra measured by ellipsometry and investigated in optical modelling. (b) Measured (blue) and modelled (red) transmission for the tri-layer MoO_3/Ag/MoO_3 anode. The absorbance (green) of a C_{70} film deposited on glass is shown for reference. (c) Measured current-voltage curves of the tri-layer anode directly after fabrication (blue) and after two weeks in air (red). The distance between the 2 electrodes was 1 mm. (For interpretation of the references to colour in this figure legend, the reader is referred to the Web version of this article.)

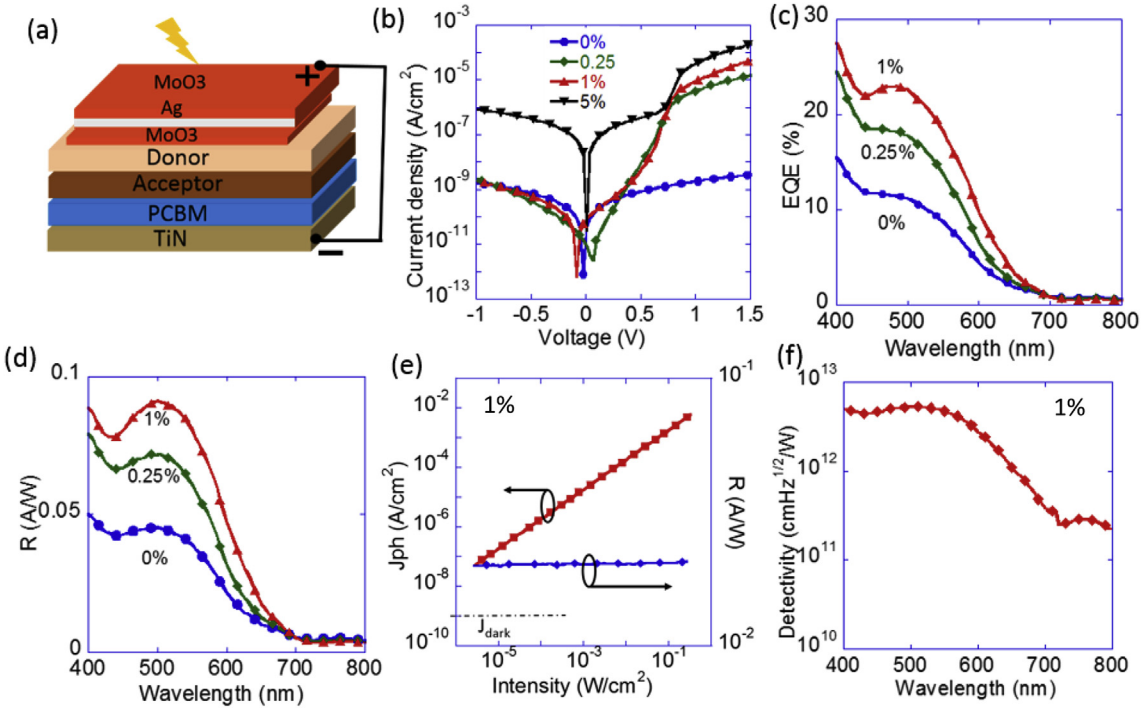

Fig. 5. (a) Schematic structure of the fabricated inverted OPDs (b) Dark current-voltage characteristics for the undoped and doped devices. (c) EQE versus wavelength of undoped and doped devices measured at 0 V. (d) Spectral responsivity of the devices at 0 V bias. (e) LDR of 1% doped device measured at −1 V under white light illumination. (f) Detectivity of 1% doped device at −1 V. Further comparison between 0% and 1% doped devices under different bias conditions can be found in Fig. S7 in the supplementary information.

device (12%). These EQE values are relatively moderate compared to solution processed semi-transparent inverted bulk heterojunction (BHJ) based devices [39,40]. In order to examine whether the performance of our photodetector devices can be enhanced by using a BHJ active layer, we fabricated and characterized the dark leakage current and EQE of such devices. For best comparison the BHJ device has the bi-layer structure with a 40 nm thick BHJ layer inserted at the bi-layer donor-acceptor interface. Supp. Info. Fig. S6a shows the EQE response of a planar BHJ active layer device of structure TiN/PCBM (80 nm)/C_{70} (40 nm)/C_{70}:TAPC (70:30 40 nm)/TAPC (50 nm)/MoO_3 (10 nm)/Ag (12 nm)/MoO_3 (32 nm) at 0 and -1 V. The EQE response of the BHJ active layer device at short circuit condition is 34% compared to 23% for a bilayer device measured at 500 nm. At −1 V the response of the BHJ device is increased to 40% compared to the 24% of the bi-layer. However, these improvements are accompanied by a significantly higher dark leakage current as compared to the bilayer device (see Supp. Info. Fig. S6b). Specifically, the measured leakage current in the BHJ active layer device at −1 V was 3×10^{-7} A/cm^2 - almost two orders higher than the bilayer device. Such a large leakage current would significantly decrease the key photodetector figures of merit, namely the detectivity and LDR, so despite the enhancements in quantum efficiency, an OPD that incorporates a BHJ active layer is still inferior to the bilayer OPD device. For solution processed BHJ OPD there are reports of low dark current and high detectivity [5,10,41,42], however these are typically much thicker devices exhibiting a low frequency response, at reverse bias not exceeding -1 V [2]. The origin of the high leakage current in our BHJ active layer device is related to the increased interfacial area in this device. We have shown that the leakage current in our bilayer devices is dictated by the junction and depends on how efficient are the recombination-generation processes at the donor/acceptor interface [43]. The high interfacial area in the BHJ active layer device means more efficient recombination-generation via interface states, which would result in enhanced leakage current. The enhanced number of interface states is also reflected by the BHJ active layer device having a higher ideality factor of n ~2.05 as compared to the bilayer device n ~1.58 (see inset Supp. Info. Fig. S6b). Moreover, we note that due to the presence of large contact barriers (1.4 eV for holes and 3.5 eV for electrons) any reverse bias contact injection can be ruled out. Based on these results solely the undoped and 1% doped bilayer devices were selected for further photodetector specific characterizations. Detailed studies of the generation-recombination processes in C_{70}:TAPC bi-layer devices can be found in the recent work by Liraz et al. [44]. Specifically, it shows that the generation is limited only by the single junction collection efficiency and that the recombination is bimolecular.

Fig. 5d shows the spectral responsivity of the undoped and doped devices at zero bias calculated using the expression:

$$R = \lambda * EQE/1240 \quad (2)$$

Where R is the responsivity (A/W), λ is the wavelength of incident light (nm) and EQE is the spectral external quantum efficiency of the device. For λ = 500 nm at 0 V, the 1% doped device shows a responsivity of 0.092 A/W, while the undoped device's responsivity is only 0.047 A/W. At −0.5 and −1 V, the responsivity of the 1% doped device increased to 0.095 A/W, 0.096 A/W, whereas the undoped device's responsivity rose to 0.056 A/W, 0.065 A/W respectively.

The photosensitive linearity measurement, also known as LDR, of the 1% doped device at −1 V under white light illumination is shown in Fig. 5e. The device shows perfect linearity in the entire measurement range of our equipment set up. The lower limit of the LDR in general defined by the noise current. At −0.5 V, dark current is the dominant source of noise in our OPD (see next paragraph). The LDR of the photodetector calculated on 20 log scale, which is given by Ref. [45].

$$\mathrm{LDR} = 20 \log_{10}(J_{Photo}/J_{Dark}) \quad (3)$$

where J_{Photo} is the upper limit of the photocurrent that is still linear with respect to the light intensity and J_{Dark} is the dark current. The optimized 1% doped device results in an LDR of at least ~135 dB and ~140 dB at −1 and −0.5 V respectively which is a high value for small molecule and polymer based OPDs [6,39].

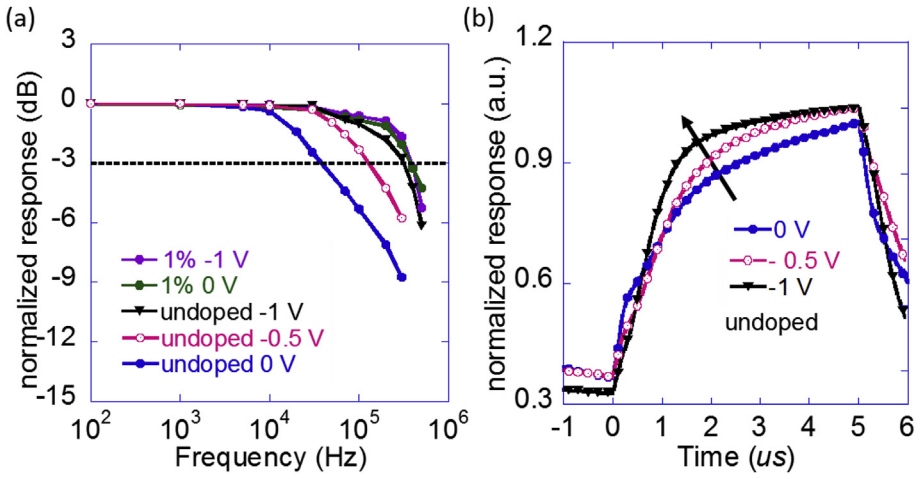

Fig. 6. (a) Frequency response of undoped and 1% doped devices measured at different voltages. The -3 dB frequency at short circuit condition for the undoped device is 38 kHz which increased to more than 300 kHz at −1 V. The 1% doped device has a relatively constant bandwidth of 388 kHz. (b) Dynamic photoresponse of the undoped device. It shows the decrease of rise time at higher reverse bias voltages.

Characterizing the photosensitivity linearity of undoped and doped devices at various biases provides insight into the origin of the improvements for the latter. Measurements performed at −0.2 V (see Supp. Info. Fig. S7a) show that while the doped device (1%) exhibits a linear response over the entire intensity range, the undoped device's response deviates from linearity at high intensities. This deviation from linearity is reduced when a higher voltage of −0.4 V is applied (see Supp. Info. Fig. S7b). This suggests that in the case of undoped PCBM devices, a significant voltage drops across the PCBM layer, reducing the electric field available to assist with charge separation and extraction. Applying a higher bias resolves this issue by increasing the electric field, until at -1 V bias the linearity of the photosensitivity response is restored (See Supp. Info. Fig. S7c). This effect is also evident in the EQE measurements at −1 V bias when compared to EQE at 0 V. While no significant change can be seen for the doped devices, the EQE of the undoped device increases from 12% to 16% (see Supp. Info Fig. S7d). These results highlight that the high performance of the doped OPD is compatible with operation at low voltages (below 1 V), which would also lower the leakage current and enhance the device sensitivity.

To quantify the optimized OPDs noise, first noise equivalent power (NEP) was calculated. NEP is defined as the minimum light power required in order to generate an electrical signal equivalent to the noise current of the photodetector at a specific bandwidth (B) is given by Ref. [46].

$$NEP = I_{noise}/R \tag{4}$$

where R is the responsivity (A/W) at specific wavelength and I_{noise} (A/$Hz^{1/2}$) is the noise current defined as [45].

$$I_{noise} = \left[2eJ_{dark}B + \frac{4KTB}{R_{sh}}\right]^{0.5} \tag{5}$$

where e is the absolute electron charge (1.6×10^{-19} C), J_{Dark} is the dark current (A), B is the detection bandwidth (Hz), K is the Boltzmann constant, T is the temperature, and R_{sh} is the effective shunt resistance, representing the leakage current, of the photodiode (ohm). We note that Eq. (5) does not count other sources of noise such as flicker noise. With the typical values of our 1% doped device at −0.5 V ($J_{Dark} = 1.1 \times 10^{-10}$ A, $B = 1$ Hz and $R_{sh} \sim 5.5G\Omega$) the calculated shot noise current of 6×10^{-15} A/$Hz^{1/2}$ was higher than the thermal noise of 1.7×10^{-15} A/$Hz^{1/2}$. The effective shunt resistance was approximated from the diode's J-V curve (see the Suppl. Info. Fig. S8). Using Eq. (4) the calculated shot noise equivalent NEP for 500 nm wavelength light is $\sim 5.6 \times 10^{-14}$ W/$Hz^{1/2}$. Area independent noise figure also known as specific detectivity (D^*) for a photodiode is given by

$$D^* = \sqrt{A}/NEP = R\sqrt{AB}/\sqrt{2qJ_{dark}} \tag{6}$$

where A is the device area (cm^2) and rest of the parameters have their usual meaning as mentioned before. Eq. (6) is valid under the assumption that the dark leakage current of the OPD is the dominant source of noise. As we showed in the last section that at −0.5 V, the calculated shot noise was found to be higher than the thermal noise. At 500 nm under −0.5 V, −1 V bias, the detectivity of 1% doped devices is found to be 7.15×10^{12} and 5.28×10^{12} Jones respectively. The undoped device whereas showed a detectivity of 3.5×10^{12} Jones and 3.42×10^{12} Jones at −0.5 V and −1 V respectively. A spectral detectivity characteristics at −1 V for 1% doped device is presented in Fig. 5f. We note that above detectivity values were calculated in a 1 Hz bandwidth.

As the final figure of merit we characterized the frequency response of the undoped and 1% doped devices. The cut-off frequency or the bandwidth was determined by the frequency of input light modulation at which the photodiode response is -3 dB lower than the low frequency signal. An alternative method to characterize the photodiode's speed is to quantify its rise or fall times. The rise time is defined as the time it takes the output signal to increase from 10% to 90% of the final output level. The -3 dB frequency for the undoped and 1% doped device at different reverse bias conditions are shown in Fig. 6a. At short circuit condition the -3 dB frequency for the undoped device was found to be 38 kHz whereas 1% doped device showed a much higher cut-off frequency of 388 kHz. This high bandwidth achieved in 1% doped device is more than enough for imaging applications such as required in digital still cameras and scan cameras [47]. In the case of the undoped device the cut-off frequency gradually increased to ~ 310 kHz at −1 V. Whereas in the case of 1% doped device no bias dependent response improvement was observed. This cut-off frequency improvement of the undoped device can also be seen as the increase in the rise time of the device (see Fig. 6b).

The frequency response of a photodiode is limited by either the carrier transit time or the RC time constant [48]. Our results indicate that the cut-off frequency of the doped OPDs is limited by the characteristic RC time constant and not by the transport across the diode. The undoped OPD, however, is limited by the transport across the undoped PCBM layer as is also supported by the very low forward current in Fig. 5b. At higher voltages, the bandwidth is no longer limited by the undoped PCBM layer and begins to approach the RC limit.

3.5. Impact of environmental conditions on device performance and compatibility with CMOS processing

The environmental stability of the devices was assessed by characterizing them directly after fabrication in an inert environment and after storage in ambient air in the dark without encapsulation. Fig. 7a shows the dark current characteristics of a fresh device and the same device after 2 weeks in the air. The forward current at 1.5 V has

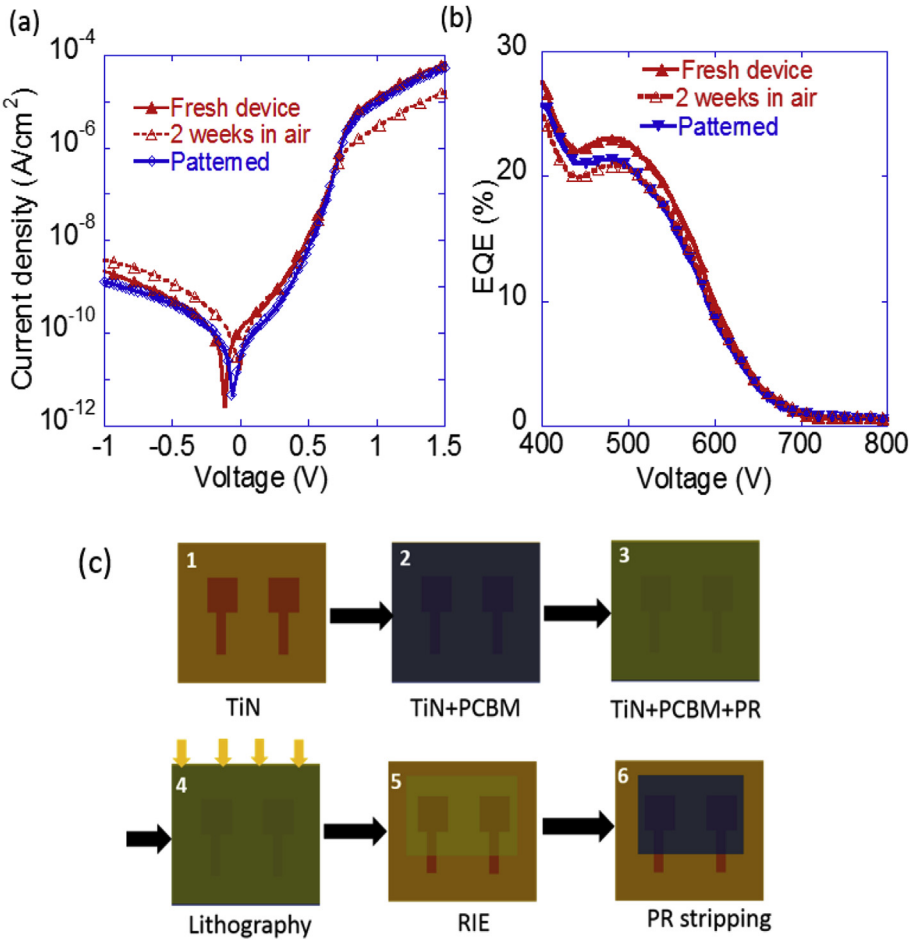

Fig. 7. (a) Dark current-voltage characteristics of a fresh device (solid red), same non encapsulated device after 2 weeks storage in ambient atmosphere (dotted red) and a patterned device (blue). (b) Spectral EQE response of the same devices. (c) Schematics of patterned devices going through additional processing steps, compared to an unpatterned device. (For interpretation of the references to colour in this figure legend, the reader is referred to the Web version of this article.)

decreased from 66 μA/cm^2 to 16 μA/cm^2, but more importantly the reverse bias leakage current at −1 V changed only slightly from ~2 nA/cm^2 to ~4 nA/cm^2. The corresponding EQE measurements (Fig. 7b) show that there was no significant degradation in the optical response of the device.

Furthermore, to investigate the feasibility of integrating the OPD device structure on CMOS readout circuits, the PCBM layer was patterned prior to the fabrication of an OPD over it. Patterning allows using a specific area of the substrate for OPD, leaving the rest of the substrate area for other purposes, for example, for readout circuitry and external bonding for device characterization. Fig. 7a shows the dark current characteristics of a device in which the PCBM layer has gone through lithography and reactive ion etching processes. The patterned device shows excellent qualities and has a similar level of dark current (~1 nA/cm^2 at −1 V) and EQE - as shown in Fig. 7b – compared to the unpatterned device. This result indicates that the doped PCBM layer retains its properties after lithography, etching, and photoresist stripping processing steps (see Fig. 7c and Supp. Info Fig. S9) making it compatible with CMOS processing. We note that these process steps were done on the test blanket substrate Si/SiO_2/TiN. In the next step these processes including OPD integration will be carried out on real CMOS ROIC which is currently under investigation and will be published elsewhere. Finally, the calculated in-plane parasitic current (see Supp. Info) of 1% doped PCBM film was almost two orders of magnitude below the diode leakage current which eliminates the need for isolating PCBM coated pixel pads.

4. Conclusion

In summary, TiN was explored and successfully implemented as bottom electrode in an inverted top-illuminated OPD. We have shown that a sandwiched interlayer of N-DMBI doped PCBM is beneficial in improving the electrical contact between TiN and the active layer (C_{70}). The other beneficial doping effect in comparison to the undoped layer is loss reduction of photogenerated carriers at low operating voltages due to much improved electron transport within the device. The optimized device shows an excellent PD characteristics, having a dark leakage current of ~6×10^{-10} A/cm^2, detectivity of 7.15×10^{12} Jones at 500 nm, linear dynamic range close to 140 dB, and negligible in-plane parasitic current at −0.5 V. Its bandwidth, although limited by the RC, is 388 kHz which is amongst the highest reported for organic PDs at below −1 V operation [49,50]. The robustness of the doped PCBM layer shows remarkable promise for future integration of OPD devices into CMOS readout circuits and potential application in high-performance large-scale array imagers.

Acknowledgements

This research was supported by the Israel Science Foundation (grant no. 488/16). We thank Mr. Dima Peselev and Dr. Orna Ternyak for their help with the lithography and RIE process steps. We thank Dr. Guy Ankonina for the ellipsometry evaluation and Dr. Cecile Saguy for the KPFM measurement. H. S. acknowledges support by the Technion Ollendorff Minerva Center. O.S. acknowledges for the support by the

Center for Absorption in Science of the Ministry of Immigrant Absorption under the framework of the KAMEA Program. Part of the device fabrication process was performed at the Technion's micro-nano fabrication and printing unit (MNF&PU).

Appendix A. Supplementary data

Supplementary data to this article can be found online at https://doi.org/10.1016/j.orgel.2019.01.002.

References

[1] J. v V R D, A. Ardalan, P.A.K, B.P.L, M. Paul, Adv. Mater. 28 (2016) 4766.
[2] K.-J. Baeg, M. Binda, D. Natali, M. Caironi, Y.-Y. Noh, Adv. Mater. 25 (2013) 4267.
[3] X. Liu, Y. Lin, Y. Liao, J. Wu, Y. Zheng, J. Mater. Chem. C 6 (2018) 3499.
[4] F.P. García de Arquer, A. Armin, P. Meredith, E.H. Sargent, Nat. Rev. Mater. 2 (2017) 16100.
[5] I. Deckman, P.B. Lechêne, A. Pierre, A.C. Arias, Org. Electron. 56 (2018) 139.
[6] D.-S. Leem, K.-H. Lee, K.-B. Park, S.-J. Lim, K.-S. Kim, Y.W. Jin, S. Lee, Appl. Phys. Lett. 103 (2013) 043305.
[7] X. Gong, M. Tong, Y. Xia, W. Cai, J.S. Moon, Y. Cao, G. Yu, C.-L. Shieh, B. Nilsson, A.J. Heeger, Science 325 (2009) 1665.
[8] F. Arca, M. Sramek, S.F. Tedde, P. Lugli, O. Hayden, IEEE J. Quant. Electron. 49 (2013) 1016.
[9] T. Rauch, S.F. Tedde, J. Furst, O. Hayden, Nat. Photon. 3 (2009) 332.
[10] A. Pierre, A. Gaikwad, A.C. Arias, Nat. Photon. 11 (2017) 193.
[11] T. Someya, Y. Kato, I. Shingo, Y. Noguchi, T. Sekitani, H. Kawaguchi, T. Sakurai, IEEE Trans. Electron. Dev. 52 (2005) 2502.
[12] G.H. Gelinck, A. Kumar, D. Moet, J. L. P. J. v. d. Steen, A. J. J. M. v. Breemen, S. Shanmugam, A. Langen, J. Gilot, P. Groen, R. Andriessen, M. Simon, W. Ruetten, A.U. Douglas, R. Raaijmakers, P.E. Malinowski, K. Myny, IEEE Trans. Electron. Dev. 63 (2016) 197.
[13] S. Tedde, E.S. Zaus, J. Furst, D. Henseler, P. Lugli, IEEE Electron. Device Lett. 28 (2007) 893.
[14] M. Mori, Y. Hirose, M. Segawa, I. Miyanaga, R. Miyagawa, T. Ueda, H. Nara, H. Masuda, S. Kishimura, T. Sasaki, Y. Kato, Y. Imada, H. Asano, H. Inomata, H. Koguchi, M. Ihama, Y. Mishima, Presented at 2013 Symposium on VLSI Technology, 11-13 June 2013, 2013.
[15] G. Zentai, IEEE International Conference on Imaging Systems and Techniques 2011, 2011, https://doi.org/10.1109/IST.2011.5962217194.
[16] V.K. Agarwala, T. Fort, Surf. Sci. 54 (1976) 60.
[17] F.P. Fehlner, N.F. Mott, Oxid. Metals 2 (1970) 59.
[18] D. Baierl, L. Pancheri, M. Schmidt, D. Stoppa, G.-F. Dalla Betta, G. Scarpa, P. Lugli 3 (2012) 1175.
[19] P. Yen, Y. Lin, S. Yu, S. Lou, K. Chuang, B. Chuang, Y. Chiou, C. Hsieh, 2016 IEEE SENSORS (2016), https://doi.org/10.1109/ICSENS.2016.7808480194.
[20] M.N. Solovan, V.V. Brus, E.V. Maistruk, P.D. Maryanchuk, Inorg. Mater. 50 (2014) 40.
[21] B. Subramanian, M. Jayachandran, Transactions of the IMF 86 (2008) 62.
[22] P. Malinowski, E. Georgitzikis, J. Maes, I. Vamvaka, F. Frazzica, J. Van Olmen, P. De Moor, P. Heremans, Z. Hens, D. Cheyns, Sensors 17 (2017) 2867.
[23] S. Lattante, Electronics 3 (2014) 132.
[24] W. Zhang, S. Pathak, N. Sakai, T. Stergiopoulos, P.K. Nayak, N.K. Noel, A.A. Haghighirad, V.M. Burlakov, D.W. deQuilettes, A. Sadhanala, W. Li, L. Wang, D.S. Ginger, R.H. Friend, H.J. Snaith, Nat. Commun. 6 (2015) 10030.
[25] C.M. Benavides, M. Biele, O. Schmidt, C.J. Brabec, S.F. Tedde, IEEE Trans. Electron. Dev. 65 (2018) 1516.
[26] R. Stephan, M. Christian, A. T D, Adv. Funct. Mater. 24 (2014) 7116.
[27] P. Wei, J.H. Oh, G. Dong, Z. Bao, J. Am. Chem. Soc. 132 (2010) 8852.
[28] C.I. Enriquez-Flores, E. Cruz-Valeriano, A. Gutierrez-Peralta, J.J. Gervacio-Arciniega, E. Ramírez-Álvarez, E. Leon-Sarabia, J. Moreno-Palmerin, Surf. Eng. (2017), https://doi.org/10.1080/02670844.2017.13852331.
[29] N.D. Treat, N. Yaacobi-Gross, H. Faber, A.K. Perumal, D.D.C. Bradley, N. Stingelin, T.D. Anthopoulos, Appl. Phys. Lett. 107 (2015) 013301.
[30] L. B, R. M, L. K, Phys. Status Solidi 210 (2013) 9.
[31] G. Weiying, K. Antoine, J. Phys. Condens. Matter 15 (2003) S2757.
[32] Y. Vaynzof, D. Kabra, L. Zhao, L.L. Chua, U. Steiner, R.H. Friend, ACS Nano 5 (2011) 329.
[33] R. Nakanishi, A. Nogimura, R. Eguchi, K. Kanai, Org. Electron. 15 (2014) 2912.
[34] D.-T. Nguyen, S. Vedraine, L. Cattin, P. Torchio, M. Morsli, F. Flory, J.C. Bernède, J. Appl. Phys. 112 (2012) 063505.
[35] S. N P, H. Afshin, N. Bjoern, C. David, H. Paul, P. Peter, R. B P, Adv. Mater. 24 (2012) 728.
[36] M. Jens, H. Sami, K. Michael, K. Wolfgang, R. Thomas, K. Antoine, Adv. Mater. 24 (2012) 5408.
[37] H. Shekhar, L. Tzabari, O. Solomeshch, N. Tessler, J. Appl. Phys. 120 (2016) 155501.
[38] S.S. Kim, S. Bae, W.H. Jo, Chem. Commun. 51 (2015) 17413.
[39] D.-S. Leem, K.-H. Lee, Y.-N. Kwon, D.-J. Yun, K.-B. Park, S.-J. Lim, K.-S. Kim, Y.W. Jin, S. Lee, Org. Electron. 24 (2015) 176.
[40] H. Kim, K.-T. Lee, C. Zhao, L.J. Guo, J. Kanicki, Org. Electron. 20 (2015) 103.
[41] T.N. Ng, W.S. Wong, M.L. Chabinyc, S. Sambanadan, R.A. Street, Appl. Phys. Lett. 92 (2008).
[42] M. Biele, C. Montenegro Benavides, J. Hürdler, S. F. Tedde, C. J. Brabec, O. Schmidt, Adv. Mater. Technol. 0, 1800158.
[43] H. Shekhar, O. Solomeshch, D. Liraz, N. Tessler, Appl. Phys. Lett. 111 (2017) 223301.
[44] D. Liraz, H. Shekhar, L. Tzabari, N. Tessler, J. Phys. Chem. C (2018), https://doi.org/10.1021/acs.jpcc.8b06404.
[45] A. Armin, M. Hambsch, I.K. Kim, P.L. Burn, P. Meredith, E.B. Namdas, Laser Photon. Rev. 8 (2014) 924.
[46] S.M. Sze, K.N. Kwok, Physics of Semiconductor Devices, WILEY, 2006.
[47] D. Baierl, L. Pancheri, M. Schmidt, P. Lugli, G. Scarpa, Nat. Commun. 3 (2012) 1175.
[48] K. Kato, IEEE Trans. Microw. Theor. Tech. 47 (1999) 1265.
[49] S.B. Lim, C.H. Ji, I.S. Oh, S.Y. Oh, J. Mater. Chem. C 4 (2016) 4920.
[50] M. Ramuz, L. Bürgi, C. Winnewisser, P. Seitz, Org. Electron. 9 (2008) 369.